

Strongly frustrated triangular spin lattice emerging from triplet dimer formation in honeycomb Li_2IrO_3

Satoshi Nishimoto,¹ Vamshi M. Katukuri,¹ Viktor Yushankhai,^{2,3} Hermann Stoll,⁴ Ulrich K. Röbber,¹ Liviu Hozoi,¹ Ioannis Rousochatzakis,^{1,3} and Jeroen van den Brink^{1,5}

¹*Institute for Theoretical Solid State Physics, IFW Dresden, Helmholtzstrasse 20, 01069 Dresden, Germany*

²*Joint Institute for Nuclear Research, Joliot-Curie 6, 141980 Dubna, Russia*

³*Max-Planck-Institut für Physik komplexer Systeme, Nöthnitzer Str. 38, 01187 Dresden, Germany*

⁴*Institute for Theoretical Chemistry, Universität Stuttgart, Pfaffenwaldring 55, 70550 Stuttgart, Germany*

⁵*Department of Physics, Technical University Dresden, Helmholtzstr. 10, 01069 Dresden, Germany*

(Dated: March 27, 2014)

In quantum magnetism spin dimers are typically associated with spin-singlet states. To date, *triplet dimerization* has not been observed in any 3D or quasi-2D material. With this in mind we here discuss the electronic structure of the spin-orbit driven $5d^5$ Mott insulator Li_2IrO_3 , a honeycomb-lattice system with two crystallographically inequivalent Ir-Ir bonds. From *ab initio* many-body calculations we find that, while both Heisenberg and Kitaev couplings are present, the magnetic interactions are dominated by a strong isotropic ferromagnetic exchange on only one set of bonds. This causes the formation of triplet spin dimers effectively placed on a strongly frustrated triangular lattice. The triplet dimers remain protected in a large region of the phase diagram, suggesting that Li_2IrO_3 has a long-range incommensurate magnetic ground state that is pushed by the Kitaev exchange interactions beyond a standard planar helix configuration.

Introduction — Low dimensionality, low spin quantum numbers, and frustrated spin-spin interactions constitute basic ingredients for exotic magnetic ground states (GS's) such as spin liquid and topologically ordered states. Of particular interest in this context is the Kitaev spin model [1], with highly anisotropic exchange interactions for spins $1/2$ on a honeycomb lattice. It hosts nontrivial spin-liquid and topological phases with elementary excitations displaying Majorana statistics, relevant for applications in topological quantum computing [2]. As a potential realization of the spin-liquid state, the strongly spin-orbit coupled honeycomb iridates $A_2\text{IrO}_3$ have been singled out, with A either Na or Li [3]. Both systems, however, have been found experimentally to order antiferromagnetically below 15 K [4, 5]. But while inelastic neutron scattering [6], x-ray and neutron diffraction [7], and resonant inelastic x-ray scattering experiments [8] indicate a zigzag antiferromagnetic (AF) pattern in Na_2IrO_3 , the nature of the AF GS of Li_2IrO_3 is to date unknown [4, 5]. The questions that arise are therefore (i) which magnetic instability preempts its spin-liquid state formation and (ii) how close the system remains to a spin-liquid GS.

To answer these fundamental questions it is essential to quantify the nearest-neighbor (NN) Heisenberg and Kitaev interactions in Li_2IrO_3 . The observed zigzag order in its counterpart system Na_2IrO_3 was rationalized on the basis of ferromagnetic (FM) Heisenberg J and AF Kitaev K couplings [10], but also interpreted in terms of an AF J and FM K [4, 6, 11]. Indeed recent *ab initio* many-body calculations indicate a relatively large FM Kitaev exchange and significantly weaker AF NN Heisenberg interactions in this material [12]. Additionally, strongly frustrating longer-range exchange couplings involving the second (J_2) and third (J_3) iridium coordination shells were also shown to become relevant [4, 6], resulting in a very rich magnetic phase diagram [4, 12, 13]. Based on the similarity in crystal structure, one might naively

expect that the magnetic interactions and GS in $A=\text{Li}$ are similar to the ones in $A=\text{Na}$. Here we show that this is not at all the case. The strengths of the NN interactions J and K turn out to crucially depend on the Ir-O-Ir bond-angles and distances. Employing *ab initio* wave-function quantum chemistry (QC) methods, we find in particular that, in contrast to Na_2IrO_3 [12], the Heisenberg coupling J in Li_2IrO_3 even has *opposite signs* on the two crystallographically inequivalent Ir-Ir links. This behavior follows a general trend of J and K as a function of bond-angle and distance that we have established through a larger, additional set of QC calculations. The latter show that the NN Heisenberg J has a parabolic dependence on the Ir-O-Ir bond-angle and at around 98° changes

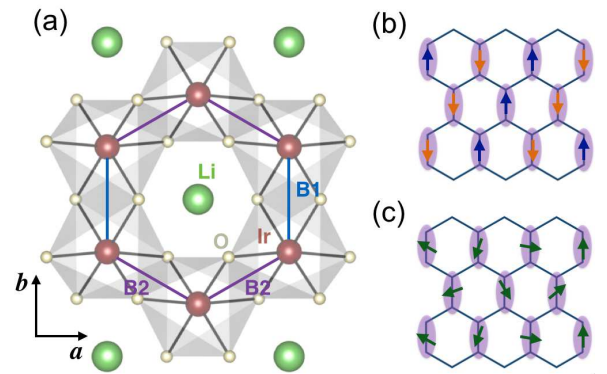


FIG. 1. (a) Honeycomb layer in Li_2IrO_3 . The two different sets of Ir-Ir links [9] are labeled as $B1$ (along the crystallographic b axis) and $B2$. (b)-(c) The large FM coupling $J_1 = -19.2$ meV on the $B1$ bonds stabilizes rigid $T = 1$ triplets that remain well protected in a wide region of the phase diagram, including the diagonal-zigzag (b) and the incommensurate ICx phase (c), see text.

sign. This explains why in Na_2IrO_3 , with Ir-O-Ir angles in the range of $98\text{--}100^\circ$ [6], all J 's are positive, while in Li_2IrO_3 , which has significantly smaller bond-angles $\sim 95^\circ$ [9], the FM component to the Heisenberg exchange is much stronger. The strong FM coupling $J \simeq -19$ meV on one set of bonds in Li_2IrO_3 gives rise to the formation of triplet dimers that form a triangular lattice. To determine the magnetic phase diagram as a function of second and third neighbor exchange interactions (J_2 and J_3) for this effective triplet-dimer model we use a semiclassical approach, which we compare to the magnetic phase diagram for the original honeycomb Hamiltonian [4, 6, 12, 13] calculated by exact cluster diagonalization. This comparison shows that indeed the triplet dimers act as rigid objects in a wide range of the J_2 - J_3 parameter space. By comparing to recent experimental observations [4, 5, 14] we can localize Li_2IrO_3 in a part of the phase diagram that has incommensurate magnetic order, the nature of which goes beyond the standard flat helix modulation scenario, owing to the Kitaev exchange anisotropy.

Ab initio QC calculations — For the electronic-structure investigations we employ multireference configuration-interaction (MRCI) calculations [15] on embedded clusters made of two edge-sharing IrO_6 octahedra. Multiconfiguration reference wavefunctions were first generated by complete-active-space self-consistent-field (CASSCF) calculations [15]. The active space is here given by five electrons and three (t_{2g}) orbitals at each of the two Ir sites. The orbitals were optimized for an average of the lowest nine singlet and the nine triplet states. All these states entered the spin-orbit calculations. In MRCI, single and double excitations from the Ir t_{2g} shells and the $2p$ orbitals of the bridging ligands are further accounted for. A similar strategy of explicitly dealing

TABLE I. Splittings among the four low-lying magnetic states and effective exchange couplings (meV) for two NN IrO_6 octahedra in Li_2IrO_3 . Results of both CASSCF and MRCI spin-orbit calculations are shown. The experimental crystal structure of Ref. [9] is used, see text. The Φ_1 - Φ_2 mixing in Ψ_1 and Ψ_2 is approximately 15%–85%, where $\Phi_1 = (\uparrow\downarrow + \downarrow\uparrow)/\sqrt{2}$ and $\Phi_2 = (\uparrow\uparrow + \downarrow\downarrow)/\sqrt{2}$ (see SM).

Method	CASSCF+SOC	MRCI+SOC
<i>B1</i> , $\angle(\text{Ir-O-Ir})=95.3^\circ$, $d(\text{Ir-Ir})=2.98 \text{ \AA}$ ($\times 1$) ^a :		
Ψ_2	0.0	0.0
$\Psi_3 = \Phi_3 = (\uparrow\uparrow - \downarrow\downarrow)/\sqrt{2}$	1.6	3.2
Ψ_1	5.4	7.7
$\Psi_S = \Phi_S = (\uparrow\downarrow - \downarrow\uparrow)/\sqrt{2}$	25.5	24.8
$(J, K, \Gamma_{xy}, \Gamma_{zx} = -\Gamma_{yz})$ ^b		
		(-19.2, -6.0, -1.1, -4.8)
<i>B2</i> , $\angle(\text{Ir-O-Ir})=94.7^\circ$, $d(\text{Ir-Ir})=2.98 \text{ \AA}$ ($\times 2$) ^c :		
$\Psi_3 = \Phi_3 = (\uparrow\uparrow - \downarrow\downarrow)/\sqrt{2}$	0.0	0.0
Ψ_2	2.8	3.7
$\Psi_S = \Phi_S = (\uparrow\downarrow - \downarrow\uparrow)/\sqrt{2}$	5.9	7.1
Ψ_1	5.7	8.4
$(J, K, \Gamma_{xy}, \Gamma_{zx} = -\Gamma_{yz})$ ^d		
		(0.8, -11.6, 4.2, -2.0)

^a $d(\text{Ir-O}_{1,2})=2.01 \text{ \AA}$. O_1 and O_2 are the two bridging O's.

^b MRCI+SOC. SOC stands for spin-orbit coupling.

^c $d(\text{Ir-O}_1)=2.08 \text{ \AA}$, $d(\text{Ir-O}_2)=1.97 \text{ \AA}$.

^d MRCI+SOC.

only with selected groups of localized ligand orbitals was earlier adopted in QC studies on both $3d$ [16] and $5d$ [12, 17–20] compounds, with results in good agreement with the experiment [16–19].

As shown in Ref. [12], the relevant effective spin Hamiltonian for a pair of NN Ir d^5 sites is

$$\mathcal{H}_{ij}^{C_{2h}} = J \tilde{\mathbf{S}}_i \cdot \tilde{\mathbf{S}}_j + K \tilde{S}_i^z \tilde{S}_j^z + \sum_{\alpha \neq \beta} \Gamma_{\alpha\beta} (\tilde{S}_i^\alpha \tilde{S}_j^\beta + \tilde{S}_i^\beta \tilde{S}_j^\alpha), \quad (1)$$

where $\tilde{\mathbf{S}}_i$, $\tilde{\mathbf{S}}_j$ are pseudospin operators, J is the isotropic Heisenberg interaction, K the Kitaev coupling [1, 3], the $\Gamma_{\alpha\beta}$ coefficients define the symmetric anisotropic tensor, with $\alpha, \beta \in \{x, y, z\}$, and the *local* reference frame $\{x, y, z\}$ is such that z is perpendicular onto the Ir_2O_2 plaquette [3, 12]. For C_{2h} symmetry of the Ir-Ir link, $\Gamma_{zx} = -\Gamma_{yz}$ [12]. The experimental data reported in Ref. [9] indicate C_{2h} symmetry for one type of Ir-Ir links, denoted as *B1* in Fig. 1, and some deviations from C_{2h} for the other type of pair of Ir NN's, labeled *B2* in Fig. 1.

Relative energies for the four low-lying states describing the magnetic spectrum of two NN octahedra [12] and the resulting effective coupling constants are listed in Table I. To determine the nature of each spin-orbit state we explicitly compute the dipole and quadrupole transition matrix elements within that manifold. A careful symmetry analysis reveals that the spin-orbit wave functions Ψ_S , Ψ_1 , Ψ_2 , and Ψ_3 defined in Table I transform in C_{2h} point-group symmetry according to the A_g , B_u , B_u , and A_u irreducible representations, respectively. Standard selection rules and the nonzero dipole and quadrupole matrix elements in the QC outputs then clearly indicate which state is which. We also carried out the

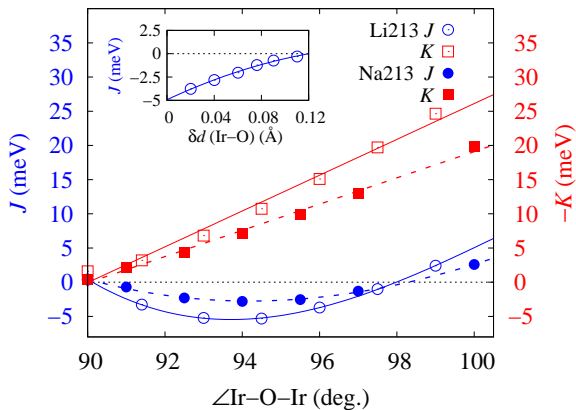


FIG. 2. Dependence of the NN J and K on the Ir-O-Ir bond angle in idealized structural models of both Li_2IrO_3 (continuous lines) and Na_2IrO_3 (dashed). MRCI+SOC results. For each system, the Ir-Ir distances are set to the average value in the experimental crystal structure [6, 9] and the Ir-O bond lengths are all the same. The variation of the Ir-O-Ir angles is the result of trigonal compression. Note that $|J|, |K| \lesssim 1$ at 90° . Inset: dependence of the NN J in Li_2IrO_3 when the bridging ligands are gradually shifted in opposite senses parallel to the Ir-Ir axis.

transformation of the spin-orbit wave functions from the usual $\{L_1, M_{L_1}, L_2, M_{L_2}, S, M_S\}$ basis in standard QC programs to the $\{\tilde{S}_1, \tilde{S}_2, \tilde{M}_{S_1}, \tilde{M}_{S_2}\}$ basis. This allows the study of Φ_1 – Φ_2 mixing due to the Γ_{yz} and Γ_{zx} couplings, as discussed in Ref. [12].

For the *B1* links in Li213 we find that both J and K are FM, in contrast to Na213, where J is AF for all pairs of Ir NN's [12]. Quite insightful here are the curves plotted in Fig. 2, displaying the dependence of the NN J on the amount of trigonal distortion for simplified structural models of both Li213 and Na213. The trigonal compression of the O octahedra translates into Ir-O-Ir bond angles larger than 90° . Additional distortions giving rise to unequal Ir-O bond lengths, see the footnotes in Table I, were not considered in these idealized lattice configurations. Interestingly, we find that for 90° bond angle – the case for which most of the superexchange models are constructed [3, 11, 21] – both J and K are very small, $\lesssim 1$ meV. Further, while $|K|$ monotonously increases with the Ir-O-Ir bond angle, J displays a parabolic behaviour and changes sign around 98° . Our investigation also shows that the large FM J value obtained for the *B1* Ir-Ir links in Li213 is the superposition of three different effects (see Fig. 2): an Ir-O-Ir bond angle smaller than the value of $\approx 98^\circ$ where J changes sign which in contrast to Na213 takes us into the FM regime, the shift to lower values of the minimum of the nearly parabolic J curve in Li213, and further the additional distortions giving rise to three different sets of Ir-O bond lengths for each IrO_6 octahedron. The latter are significantly stronger in Li213, remove the degeneracy of the Ir t_{2g} levels, and make that the NN *B1* J is even lower than the minimum of the parabola displayed in Fig. 2. It is also interesting that the offdiagonal Γ_{yz} and Γ_{zx} couplings have about the same strength with the Kitaev K (see Table I).

For the *B2* links, the Ir-O bonds on the Ir-O₂-Ir plaquette have different lengths and the symmetry of the two-octahedra block is lowered to C_i [9]. The *ab initio* data show that consequently the FM exchange is here disfavored such that J turns AF. This is illustrated in the inset of Fig. 2, where we plot the evolution of the NN J when in addition to trigonal distortions the bridging ligands on the Ir-O₂-Ir plaquette are gradually shifted in opposite senses parallel to the Ir-Ir axis. For the reference equilateral plaquette, the Ir-O-Ir bond angle is set to the average value in the experimental structure, 95° [9]. It is seen that such additional distortions indeed enhance the AF contribution to the Heisenberg superexchange. Although the bond symmetry is lower for the *B2* links, the analysis of the spin-orbit wave functions shows however negligible additional mixing effects and the *ab initio* results were still mapped onto a C_{2h} model with $\Gamma_{zx} = -\Gamma_{yz}$.

Magnetic phase diagram — Having established the dominant microscopic NN Ir-Ir couplings, we now turn to the magnetic phase diagram of Li213 including the effect of second and third neighbor Heisenberg interactions J_2 and J_3 , which are known to be important in such compounds [4, 6, 11–13]. Given the strong FM energy scale on the *B1* bonds, a natural description of the problem can be given by replacing all *B1*

pairs of spins-1/2 by rigid triplet degrees of freedom. This mapping leads to an effective spin $T = 1$ model on the triangular lattice, with onsite quadrupolar and intersite symmetric anisotropy terms, in addition to isotropic exchange. In momentum space, the corresponding effective Hamiltonian is

$$\mathcal{H}_{\text{eff}} = \sum_{\alpha, \beta, \mathbf{k}} T_{\mathbf{k}}^\alpha \cdot \Lambda_{\alpha\beta}(\mathbf{k}) \cdot T_{-\mathbf{k}}^\beta, \quad (2)$$

where $T_{\mathbf{k}} = \frac{1}{N} \sum_{\mathbf{R}} e^{i\mathbf{k} \cdot \mathbf{R}} \mathbf{T}_{\mathbf{R}}$, N is the number of *B1* bonds, and $\Lambda(\mathbf{k})$ is a symmetric 3×3 matrix (see Supplemental Material). Since $T = 1$, the classical limit is expected to give a good picture for the phase diagram. The minimum eigenvalue $\lambda_{\mathbf{Q}}$ of $\Lambda(\mathbf{k})$ over the Brillouin zone (BZ) gives a lower bound for the classical GS energy [22–25]. As shown in Fig. 3(a), there exist five different regions for $|J_{2,3}| \lesssim 6$ meV, three with commensurate (FM, diagonal zigzag and stripy) and two with incommensurate \mathbf{Q} (ICx and ICy, with $\mathbf{Q} = (q, 0)$ and $(0, q)$, respectively). In all commensurate regions, the state $\mathbf{T}_{\mathbf{R}} = e^{i\mathbf{Q} \cdot \mathbf{R}} \mathbf{v}_{\mathbf{Q}}$ (where $\mathbf{v}_{\mathbf{Q}}$ is the eigenvector associated with $\lambda_{\mathbf{Q}}$), saturates the above lower energy bound and in addition satisfies the spin length constraint $|\mathbf{T}_{\mathbf{R}}| = 1$ for all \mathbf{R} . We note in particular that compared to the more symmetric case of Na213 [12], only the *diagonal-zigzag* configurations are favored in Li213, with FM correlations along the two “diagonal” directions of the lattice. The third, “horizontal”, zigzag configuration is penalized by the strong FM Heisenberg coupling on the *B1* links. Correspondingly, we expect Bragg peaks only at two out of the three M points of the BZ, namely $\mathbf{Q} = (\pi, \pm \frac{\pi}{\sqrt{3}})$ (see $S(\mathbf{Q})$ in Fig. 3). Turning to the incommensurate regions ICx and ICy, the minimum eigenvalue $\lambda_{\mathbf{Q}}$ is nondegenerate, which implies that one *cannot* form a flat helical modulation that saturates the low energy bound and satisfies the spin length constraint for all \mathbf{R} . Especially for ICx, which is the most likely candidate for Li213 (see below), this opens the possibility for nontrivial nonplanar modulations.

To establish the effect of quantum fluctuations and further test the triplet-dimer picture, we additionally carried out exact diagonalization (ED) calculations on 24-site clusters for the original honeycomb spin-1/2 model including the effect of J_2 and J_3 . Periodic boundary conditions were applied, as in previous studies [3, 21]. We calculated the static spin structure factor $S(\mathbf{Q}) = \sum_{i,j} \langle \tilde{\mathbf{S}}_i \cdot \tilde{\mathbf{S}}_j \rangle \exp[i\mathbf{Q} \cdot (\mathbf{r}_i - \mathbf{r}_j)]$ as a function of J_2 and J_3 while fixing the NN magnetic couplings to the ones in Table I. For a given set of J_2 and J_3 values the dominant order is determined according to the wave number $\mathbf{Q} = \mathbf{Q}_{\text{max}}$ providing a maximum of $S(\mathbf{Q})$. The resulting phase diagram is given in Fig. 3(b). For each phase the real-space spin configuration and the reciprocal-space Bragg peak positions are shown. In the absence of J_2 and J_3 , the system is in a *spin liquid* phase characterized by a structureless $S(\mathbf{Q})$ (see Fig. 3(c)), which is adiabatically connected to the Kitaev liquid phase for $-K \gg J$ [3]. By switching on J_2 and J_3 , we recover most of the classical phases of the effective spin-1 model, including the ICx phase, albeit with a smaller stability region due to finite-size effects. That the 24-site cluster

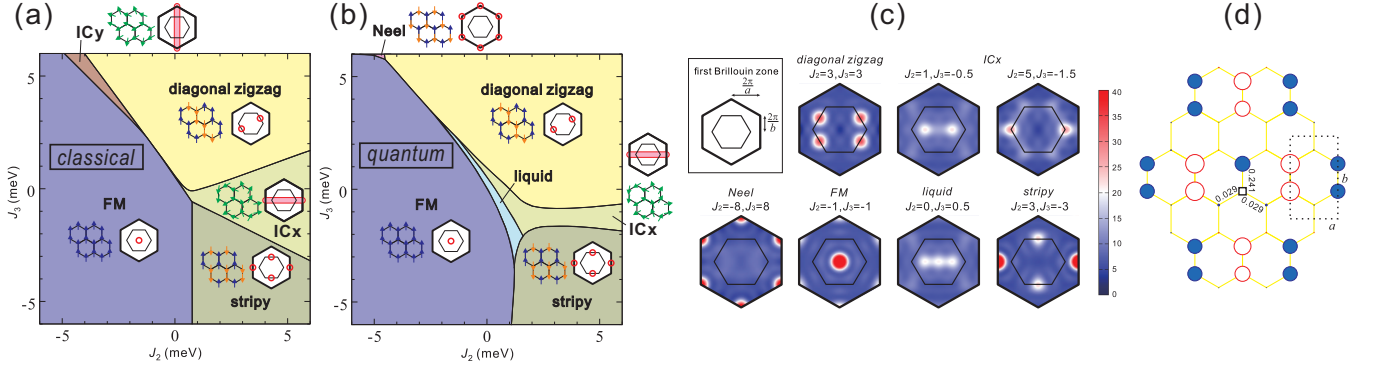


FIG. 3. Phase diagram of Li213 in the J_2 - J_3 plane with the NN $B1$ and $B2$ couplings listed in Table I, along with schematic spin configurations and Bragg peak positions (red circles) for each phase. (a) Classical phase diagram of the effective spin $T=1$ model on the triangular lattice, found by a numerical minimization of the interaction matrix $\Lambda(\mathbf{k})$ in the BZ. The actual GS configurations in the incommensurate regions ICx and ICy can be much richer than the standard coplanar helix states owing to anisotropy, see text. (b) Quantum-mechanical phase diagram for the original spin-1/2 model. (c) Structure factor $\mathcal{S}(\mathbf{k})$ for representative momenta in different phase regions. Note that in the ICx phase, the peak position $(\pm Q_a, 0)$ takes values between $0 < Q_a \leq 2\pi/a$, depending on J_2 and J_3 . (d) Long-range spin-spin correlation profiles $\langle \mathbf{S}_i \cdot \mathbf{S}_j \rangle$ in the GS at $J_2 = J_3 = 3$ (i.e., inside the diagonal-zigzag phase), as obtained by ED calculations. The reference Ir site is shown as a black square rectangle, positive (negative) correlations are denoted by filled blue (open red) circles whose radii scale with $|\langle \mathbf{S}_i \cdot \mathbf{S}_j \rangle|$. We also show explicitly the actual values for the NN correlations.

correlations do not show the ICy phase may well be an intrinsic effect, given that the classical ICy region is very narrow. We also find an AF Néel state region which is now shifted to larger J_3 's as compared to Na213 [12], due to the large negative J_{B1} . We note that detecting the diagonal-zigzag phase by ED calculations requires a large system size. That is related to the proximity of this phase to the special point $\Gamma=0$ where the model is highly frustrated. Indeed, in this limit the classical GS manifold consists of a one-parameter family of states with two sublattices of spins whose relative angle is arbitrary. This situation is common in various well-known frustrated models, such as the J_1 - J_2 model on the square lattice [26–28]. The lifting of the accidental degeneracy, either by quantum fluctuations or by the finite Γ (see Supplemental Material), and the associated locking mechanism between the two sublattices involve a very large length scale [29, 30], which is why our exact spin-spin correlation profiles provided in Fig. 3(d) show that the two sublattices are nearly decoupled from each other.

Except for the Néel and the spin liquid phase, *all* other phases feature rigid triplets on the $B1$ bonds. This is shown in Fig. 3(d) for the diagonal-zigzag phase at $J_2 = J_3 = 3$, where the NN correlation function on the $B1$ bonds, $\langle \mathbf{S}_i \cdot \mathbf{S}_j \rangle \simeq 0.24$, almost saturates the full spin-triplet value of $1/4$. This gives strong confidence that the effective triplet picture is quite robust. It finds support in recent fits of the magnetic susceptibility data, which yield effective moments of $2.22 \mu_B$ for Li213 [31], much larger than a value of $1.74 \mu_B$ expected for an isotropic 1/2 spin system. Triplet dimerization was earlier proposed to occur in the chain-like compound In_2VO_5 [32]. FM, quintet dimers were also proposed to form in ZnV_2O_4 [33].

Turning finally to the nature of the actual magnetic GS of Li213, we first note that J_2 and J_3 are expected to be not larger than 5–6 meV in honeycomb iridates [6] and AF [4, 6], which

suggests that Li213 orders either in the diagonal-zigzag or in the ICx phase. Recent magnetic susceptibility and specific heat measurements show that the GS is actually very different from zigzag [5] while inelastic neutron scattering data [14] show clear signatures of incommensurate Bragg peaks, providing strong support for the ICx spin configuration. As explained above, the actual nature of this phase goes beyond the standard flat helical modulations because the latter are penalized by the anisotropic exchange terms in the Hamiltonian.

Conclusions — We have established a microscopic spin model and zero-temperature phase diagram for the layered honeycomb iridate Li_2IrO_3 , one of the proposed realizations of the spin-1/2 Kitaev-Heisenberg model with strongly spin-orbit coupled Ir^{4+} magnetic ions. *Ab initio* quantum chemistry electronic-structure calculations show that, in contrast to Na_2IrO_3 , the structural inequivalence between the two types of Ir-Ir links has a striking influence on the effective spin Hamiltonian, leading in particular to two very different nearest-neighbor superexchange pathways, one weakly antiferromagnetic ($\simeq 1$ meV) and another strongly ferromagnetic (-19 meV). The latter gives rise to rigid spin-1 triplets on a triangular lattice that remain well protected in a large parameter regime of the phase diagram, including a diagonal-zigzag and an incommensurate ICx phase. In view of these theoretical findings and of recently reported neutron scattering data [14], we conclude that the magnetic ground state of Li_2IrO_3 lies in the incommensurate ICx phase. Establishing its detailed nature and properties calls for further, dedicated experimental and theoretical investigations.

Acknowledgements — We thank R. Coldea, Y. Singh, and D. I. Khomskii for insightful discussions. L. H. acknowledges financial support from the German Research Foundation (Deutsche Forschungsgemeinschaft, DFG).

-
- [1] A. Kitaev, *Ann. Phys.* **321**, 2 (2006).
- [2] G. Baskaran, S. Mandal, and R. Shankar, *Phys. Rev. Lett.* **98**, 247201 (2007); H.-D. Chen and Z. Nussinov, *J. Phys. A* **41**, 075001 (2008); J. Vidal, K. P. Schmidt, and S. Dusuel, *Phys. Rev. B* **78**, 245121 (2008); K. S. Tikhonov, M. V. Feigel'man, and A. Y. Kitaev, *Phys. Rev. Lett.* **106**, 067203 (2011); Z. Nussinov and J. van den Brink, arXiv:1303.5922 (unpublished).
- [3] G. Jackeli and G. Khaliullin, *Phys. Rev. Lett.* **102**, 017205 (2009); J. Chaloupka, G. Jackeli, and G. Khaliullin, *Phys. Rev. Lett.* **105**, 027204 (2010).
- [4] Y. Singh, S. Manni, J. Reuther, T. Berlijn, R. Thomale, W. Ku, S. Trebst, and P. Gegenwart, *Phys. Rev. Lett.* **108**, 127203 (2012).
- [5] G. Cao, T. F. Qi, L. Li, J. Terzic, V. S. Cao, S. J. Yuan, M. Tovar, G. Murthy, and R. K. Kaul, *Phys. Rev. B* **88**, 220414 (2013).
- [6] S. K. Choi, R. Coldea, A. N. Kolmogorov, T. Lancaster, I. I. Mazin, S. J. Blundell, P. G. Radaelli, Y. Singh, P. Gegenwart, K. R. Choi, S.-W. Cheong, P. J. Baker, C. Stock, and J. Taylor, *Phys. Rev. Lett.* **108**, 127204 (2012).
- [7] F. Ye, S. Chi, H. Cao, B. C. Chakoumakos, J. A. Fernandez-Baca, R. Custelcean, T. F. Qi, O. B. Korneta, and G. Cao, *Phys. Rev. B* **85**, 180403 (2012).
- [8] X. Liu, T. Berlijn, W.-G. Yin, W. Ku, A. Tsvelik, Y.-J. Kim, H. Gretarsson, Y. Singh, P. Gegenwart, and J. P. Hill, *Phys. Rev. B* **83**, 220403 (2011).
- [9] M. J. O'Malley, H. Verweij, and P. M. Woodward, *J. Solid State Chem.* **181**, 1803 (2008).
- [10] See, e.g., [21]. An AF NN K was also predicted in [34] for Li213.
- [11] K. Foyevtsova, H. O. Jeschke, I. I. Mazin, D. I. Khomskii, and R. Valentí, *Phys. Rev. B* **88**, 035107 (2013).
- [12] V. M. Katukuri, S. Nishimoto, V. Yushankhai, A. Stoyanova, H. Kandpal, S. K. Choi, R. Coldea, I. Rousochatzakis, L. Hozoi, and J. van den Brink, *New J. Phys.* **16**, 013056 (2014).
- [13] I. Kimchi and Y.-Z. You, *Phys. Rev. B* **84**, 180407 (2011).
- [14] R. Coldea, oral presentation at the MPI-PKS Conference *Spin Orbit Entanglement: Exotic States of Quantum Matter in Electronic Systems*, Dresden, July 22 – July 26, 2013.
- [15] T. Helgaker, P. Jørgensen, and J. Olsen, *Molecular Electronic-Structure Theory* (Wiley, Chichester, 2000).
- [16] K. Fink, R. Fink, and V. Staemmler, *Inorg. Chem.* **33**, 6219 (1994); A. B. van Oosten, R. Broer, and W. C. Nieuwpoort, *Chem. Phys. Lett.* **257**, 207 (1996); R. Broer, L. Hozoi, and W. C. Nieuwpoort, *Mol. Phys.* **101**, 233 (2003); C. J. Calzado, S. Evangelisti, and D. Maynau, *J. Phys. Chem. A* **107**, 7581 (2003).
- [17] V. M. Katukuri, H. Stoll, J. van den Brink, and L. Hozoi, *Phys. Rev. B* **85**, 220402 (2012).
- [18] V. M. Katukuri, V. Yushankhai, L. Siurakshina, J. van den Brink, L. Hozoi, and I. Rousochatzakis, arXiv:1402.3538 (unpublished).
- [19] N. A. Bogdanov, V. M. Katukuri, H. Stoll, J. van den Brink, and L. Hozoi, *Phys. Rev. B* **85**, 235147 (2012).
- [20] N. A. Bogdanov, R. Maurice, I. Rousochatzakis, J. van den Brink, and L. Hozoi, *Phys. Rev. Lett.* **110**, 127206 (2013).
- [21] J. Chaloupka, G. Jackeli, and G. Khaliullin, *Phys. Rev. Lett.* **110**, 097204 (2013).
- [22] J. M. Luttinger and L. Tisza, *Phys. Rev.* **70**, 954 (1946).
- [23] E. F. Bertaut, *J. Phys. Chem. Solids* **21**, 256 (1961).
- [24] D. B. Litvin, *Physica* **77**, 205 (1974).
- [25] T. A. Kaplan and N. Menyuk, *Philos. Mag.* **87**, 3711 (2007).
- [26] P. Chandra and B. Doucot, *Phys. Rev. B* **38**, 9335 (1988).
- [27] H. J. Schulz, T. A. L. Ziman, and D. Poilblanc, *J. Phys. I France* **6**, 675 (1996).
- [28] R. F. Bishop, D. J. J. Farnell, and J. B. Parkinson, *Phys. Rev. B* **58**, 6394 (1998).
- [29] P. Chandra, P. Coleman, and A. I. Larkin, *Phys. Rev. Lett.* **64**, 88 (1990).
- [30] C. Weber, L. Capriotti, G. Misguich, F. Becca, M. Elhajal, and F. Mila, *Phys. Rev. Lett.* **91**, 177202 (2003).
- [31] H. Lei, W.-G. Yin, Z. Zhong, and H. Hosono, *Phys. Rev. B* **89**, 020409 (2014).
- [32] S. A. J. Kimber, M. A. de Vries, J. Sanchez-Benitez, K. V. Kamenev, and J. P. Attfield, *Phys. Rev. B* **77**, 014428 (2008).
- [33] V. Pardo, S. Blanco-Canosa, F. Rivadulla, D. I. Khomskii, D. Baldomir, H. Wu, and J. Rivas, *Phys. Rev. Lett.* **101**, 256403 (2008).
- [34] H.-S. Kim, C. H. Kim, H. Jeong, H. Jin, and J. Yu, *Phys. Rev. B* **87**, 165117 (2013).